



# Strain-insensitive MXene-based wearable temperature patch with integrated thermoelectric cooling for continuous infant thermal monitoring and in-situ treatment



Xiaojiang Huang<sup>1,2</sup>, Yuan He<sup>2</sup>, Yunxiang Shi<sup>2</sup>, Yunchao Hao<sup>1</sup>, Yifan Ge<sup>3</sup>, Huiqing Zhang<sup>2</sup>✉, Peng Li<sup>2</sup>✉, Feng Xu<sup>4</sup>✉ & Yao Yao<sup>1</sup>✉

Continuous and accurate nighttime monitoring of infants' body temperature is crucial for early fever detection and timely interventions, directly impacting their health. However, existing wearable temperature sensors are often sensitive to body movement-induced strain, causing inaccurate readings, and lack integrated active temperature regulation. Here, we developed a strain-insensitive wearable temperature patch that integrates a flexible MXene-based thermal sensor with a thermoelectric cooling module for continuous monitoring and in-situ cooling treatment. The thermal sensor employs an alternating laminated architecture with interfacial interlocking, incorporating PVA/CNF/MXene/Fe(II) composites, achieving a high strain insensitivity with a gauge factor of 0.5 and high thermosensitivity with a sensitivity of  $1.78\% \text{ }^{\circ}\text{C}^{-1}$ , a resolution of  $0.5 \text{ }^{\circ}\text{C}$ , and a rapid response time of 7 s within a  $20\text{--}70 \text{ }^{\circ}\text{C}$  range. Upon fever detection, the cooling module can lower skin temperature by  $2 \text{ }^{\circ}\text{C}$ . This wearable system provides a practical solution for infant thermal management, potentially enhancing health outcomes.

Ensuring the safety and well-being of infants during nighttime is of paramount importance, as it directly impacts their overall health and development<sup>1–3</sup>. Sudden health issues such as fevers can arise quickly, requiring immediate attention to prevent complications<sup>4–7</sup>. Continuous monitoring of an infant's body temperature is crucial for early detection and timely intervention. However, conventional thermometers only provide single-point measurements and cannot offer continuous, real-time monitoring, leaving parents and caregivers vulnerable to missing potentially dangerous shifts in body temperature<sup>8,9</sup>. Therefore, this limitation highlights the need for more effective and continuous methods to monitor and regulate an infant's body temperature, especially during sleep when they are less likely to show noticeable signs of distress.

Recent advances in wearable temperature sensors have explored various thermosensitive materials, including nanomaterials (e.g., graphene<sup>10–14</sup>, carbon nanotubes<sup>15–18</sup>, and silver nanowires<sup>19</sup>), organic conductive materials (e.g., PEDOT:PSS<sup>20,21</sup> and polyaniline<sup>22,23</sup>), metallic materials (e.g., silver<sup>24,25</sup>, platinum<sup>26–28</sup>, and gold<sup>28</sup>), MXene nanosheets<sup>29–31</sup>, and other composite materials<sup>32–39</sup>. These materials have been employed to construct intrinsically stretchable conductive networks with enhanced precision and thermosensitivity. Among them, MXene nanosheets have attracted significant attention due to their excellent conductivity, mechanical strength, and processability<sup>40</sup>. Incorporating MXene into flexible substrates like polyvinyl alcohol (PVA) and reinforcing with cellulose nanofibers (CNF) can enhance mechanical flexibility and durability. However, one significant challenge in wearable temperature sensors is strain sensitivity, where mechanical

<sup>1</sup>School of Mechanics and Transportation Engineering, Northwestern Polytechnical University, Xi'an, 710072, P.R. China. <sup>2</sup>State Key Laboratory of Flexible Electronics (LoFE) & Institute of Flexible Electronics (IFE), Northwestern Polytechnical University, Xi'an, 710072, China. <sup>3</sup>Minzu University of China, 27 Zhongguancun South Street, Haidian District, Beijing, 100081, P.R. China. <sup>4</sup>Bioinspired Engineering and Biomechanics Center, The Key Laboratory of Biomedical Information Engineering of Ministry of Education, School of Life Science and Technology, Xi'an Jiaotong University, Xi'an, 710049, P.R. China.

✉ e-mail: iamhqzhang@nwpu.edu.cn; iampli@nwpu.edu.cn; fengxu@mail.xjtu.edu.cn; yaoy@nwpu.edu.cn

deformation can lead to resistance changes and negatively affect the accuracy of temperature readings<sup>41</sup>. This is particularly problematic in applications where movement is inevitable, such as infant care.

Various strategies have been employed to mitigate strain sensitivity, such as designing interlocking layered structures that lock the relative positions of layers and minimize the impact of motion interference on resistance values<sup>41,42</sup>. This approach enhances mechanical stability and improves temperature response accuracy. Despite these advancements, integrating active thermal regulation into wearable devices remains challenging for managing elevated body temperatures, such as those resulting from fever<sup>43,44</sup>. Solid-state cooling technologies, particularly thermoelectric cooling, offer promising solutions for localized fever treatment due to their simplicity, reliability, and potential for miniaturization<sup>45–51</sup>. The thermoelectric cooling can provide localized cooling without the need for compressors or refrigerants, making it suitable for wearable applications.

In our study, we designed a wearable device that integrates a flexible, strain-insensitive temperature sensor with a thermoelectric cooling module for infant care during nighttime. Our temperature sensor utilizes an alternating laminated architecture with interfacial interlocking, incorporating MXene nanosheets within a PVA/CNF composite matrix. The introduction of Fe(II) ions serves as a crosslinking agent, enhancing structural integrity without sacrificing flexibility. This design effectively minimizes strain interference, achieving a high strain insensitivity with a gauge factor of 0.5. The thermoelectric cooling module provides in-situ cooling treatment when a fever is detected, actively regulating the infant's body temperature. Our integrated device operates within a temperature range of 20–70 °C, exhibiting a sensitivity of 1.78% °C<sup>-1</sup>, a resolution of 0.5 °C, and a rapid response time of 7 s. The thermoelectric cooling module can lower skin temperature by 0.5 to 2 °C, achieving a maximum cooling efficiency of 1 °C per hour. Through finite element analysis (FEA) and experimental validation, we confirmed that our design effectively disperses stress and prevents contact between adjacent layers, reducing resistance changes due to mechanical strain. This advancement not only addresses the immediate needs of parents and caregivers by providing continuous monitoring and active temperature regulation but also contributes to the broader field of wearable biomedical devices. Our novel solution holds significant potential for improving infant healthcare and could be extended to other applications requiring precise temperature monitoring and regulation in dynamic environments.

## Results

### A laminated strain-insensitive temperature patch is fabricated using an interfacial interlocking mechanism

To address the need for continuous temperature monitoring and automatic cooling in infant night care, we developed a strain-insensitive temperature patch that enables real-time thermal monitoring, fever alerts, and in-situ cooling treatment when the forehead temperature exceeds 38 °C (Fig. 1a). The design and construction of the device consist of four main components: a thermal sensor, a cooling module, a flexible printed circuit board (FPCB), and an encapsulating layer (Fig. 1b).

The cooling module works through the Peltier effect, where thermal energy is captured or released at the connection of two different semiconductor materials when an electric charge flows through (Fig. 1c). Upon detecting a fever, the cooling module activates to provide immediate cooling treatment, ensuring the comfort of the sick infant (Fig. 1d). For precise temperature detection, we designed the thermal sensor module with an interlocking structure (Fig. 1e). It comprises alternating layers of polyvinyl alcohol (PVA), cellulose nanofibers (CNF), MXene nanosheets, and iron(II) ions (Fe(II)), forming a composite (PCM) thermosensitive layer. MXene nanosheets respond resistively to temperature variations, while PVA contributes elasticity, assuring the mechanical integrity of the sensor. The coordination bonds formed between the carboxyl groups of Fe(II) and the nanocellulose reinforce the polymer network interactions, ensuring accurate temperature measurements while maintaining strain insensitivity.

To evaluate the mechanical performance of the interlocking structure, we perform finite element analysis (FEA), which reveals that the interlocked

layers alleviate stress concentration under strain (Fig. 1f). This design leads to energy dissipation and deformation suppression (Supplementary Movie 1). At low strain levels, the lack of contact between layers prevents the formation of new conductive paths, enhancing temperature measurement accuracy. At high strain levels, new conductive paths form, reducing resistance and maintaining measurement accuracy.

Our results indicate that the strain-insensitive temperature patch effectively combines continuous thermal monitoring with in-situ cooling treatment, providing a practical solution for infant night care.

### The PVA/CNF/MXene/Fe(II) composite enhances mechanical stability and electrical conductivity

To assemble the laminated structure, we stacked individual layers and sprayed a 1 M FeCl<sub>2</sub> solution between each adjacent layer to create interfacial bridging. We applied a compression process at 20 MPa for 20 min to strengthen the interfacial interactions among MXene, CNF, and Fe(II) and to minimize interlayer voids. The resulting CNF/PVA/MXene/Fe(II) composite film, depicted in Fig. 2a, exhibits a rough surface morphology with small protrusions (Fig. 2b), which facilitate interfacial bridging. Colored SEM images (Fig. 2c and Supplementary Fig. 3) and AFM images (Supplementary Fig. 4) confirm the dense, tightly integrated lamellar structure of the composites.

We selected Fe(II) for its unique ability to form coordination bonding with the functional groups (–F, –O–, –OH) on MXene nanosheets, effectively balancing bonding strength and material stability without oxidizing MXene, unlike trivalent ions like Fe(III)<sup>52</sup>. By disrupting electrostatic repulsion, Fe(II) facilitates the assembly of a stable 3D MXene hydrogel, making it an optimal choice for our composite. MXene nanosheets, with abundant functional groups (–F, –O–, –OH), extensive surface area, exceptional mechanical strength, and excellent conductivity, are key to chemosensitivity and mechanical flexibility. To enhance conductivity and thermosensitivity, we uniformly distributed MXene within the PVA and CNF matrix (Fig. 2d and Supplementary Fig. 5), enabling efficient electron transport and precise temperature detection. TEM observations (Fig. 2e) revealed MXene's lamellar structure with elements C, O, Ti, and F (Supplementary Fig. 6), along with wrinkles and curvature indicating mechanical flexibility. The 0.25 nm lattice fringe corresponds to the Ti<sub>3</sub>C<sub>2</sub>T<sub>x</sub> (006) plane. While MXene offers excellent mechanical and conductive properties, PVA enhances overall mechanical performance and interface compatibility. However, hydrogen bonds and van der Waals forces alone may be insufficient for stable interfacial bridges between PVA and MXene layers, potentially compromising strain insensitivity. To address this, we introduced coordination interactions between metal ions and functional groups, such as the carboxyl groups (–COOH) of CNF and Fe(II), to strengthen interfacial bridges. CNF, with high aspect ratios and abundant functional groups (–OH, –COOH), further reinforces these bonds. Additionally, hydroxyl groups (–OH) on PVA molecules form hydrogen bonds with CNF and MXene, promoting dispersion and stabilization. Electrostatic interactions facilitated by these groups enhance MXene dispersion in the PVA matrix. Therefore, the strategic combination of PVA, CNF, and MXene synergistically enhances film-forming properties, mechanical strength, and electrical conductivity in the composite material.

To verify these synergistic effects, we conduct a series of characterizations. FTIR spectroscopy (Fig. 2f) revealed a diminished peak at 1608 cm<sup>-1</sup> and a new peak at 1720 cm<sup>-1</sup>, indicating metal complexation between –COOH and Fe(II). The XPS full-spectrum map (Supplementary Fig. 7) of CNF/MXene and MXene composites confirms the presence of C, O, Ti, and Fe elements, consistent with EDS mapping. High-resolution XPS spectra of O 1s and F 1s (Supplementary Fig. 7) show new peaks for Fe–O and Fe–F bonds at 531.7 eV and 685.28 eV in MXene/Fe(II), suggesting Fe(II) interaction with MXene's O and F groups, aligning with previous reports<sup>53</sup>. Ti 2p and C 1s XPS spectra (Fig. 2g, h) of MXene and MXene/CNF show positive shifts in C–Ti–OH (455.98 to 456.08 eV), C–Ti–O (456.98 to 457.08 eV), C–O (285.48 to 285.68 eV), and Ti–O (456.98 to 457.08 eV) bonds, reflecting

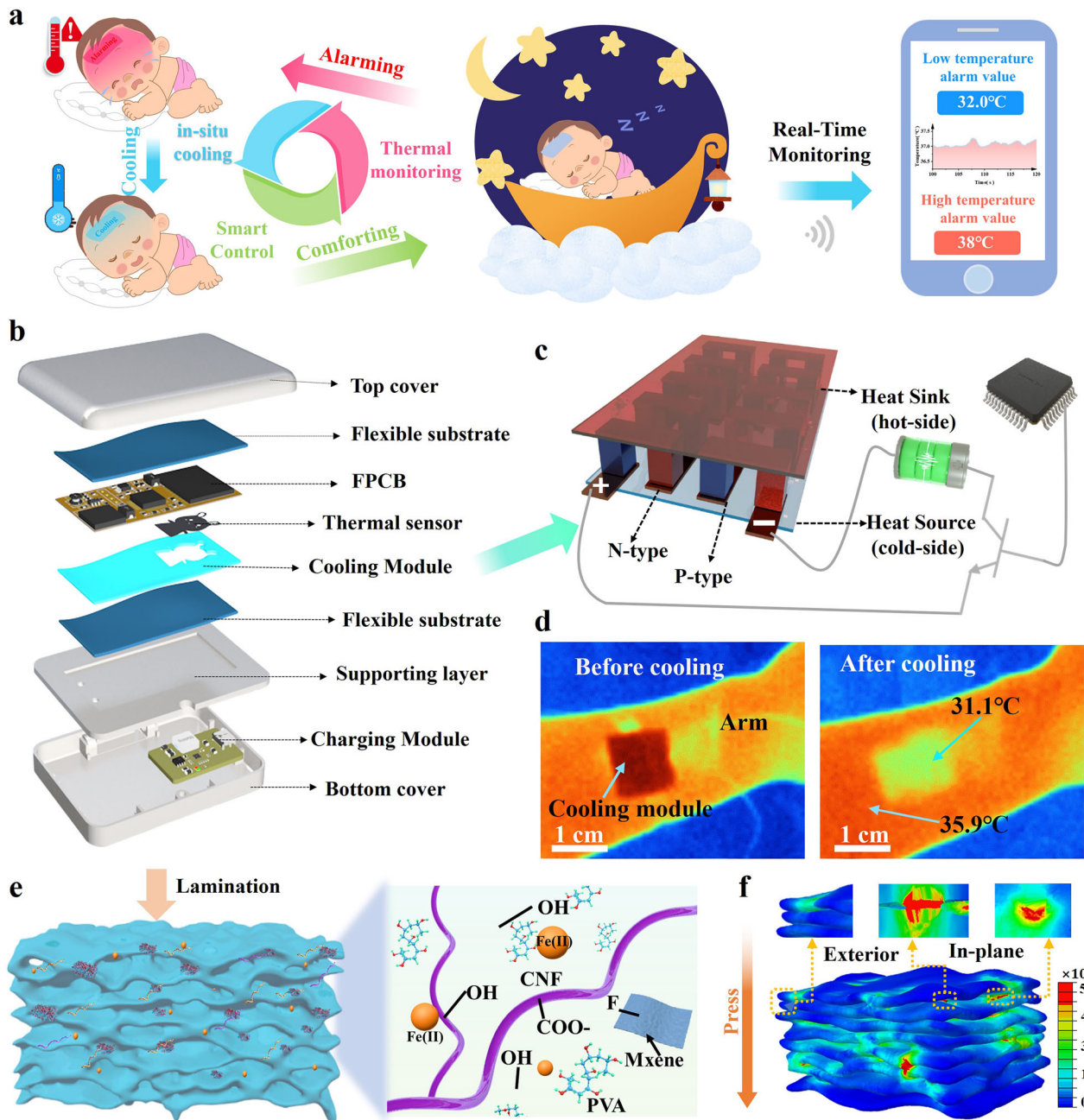
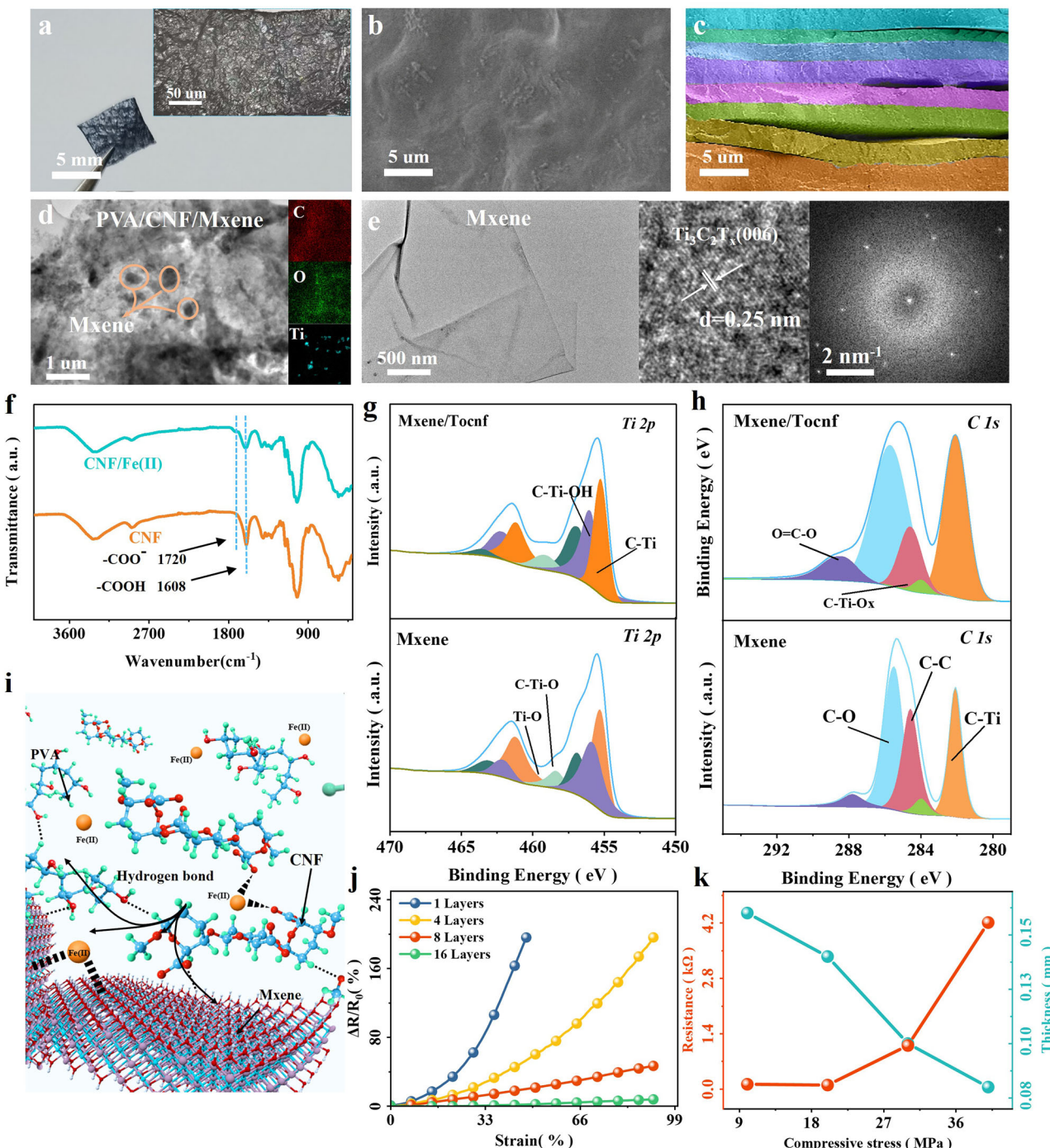


**Fig. 1 | Schematic of the strain-insensitive temperature patch for infant night care on thermal monitoring and in-situ cooling treatment.** **a** Applications of the wearable patch for body temperature monitoring, fever alarming, and in-situ cooling treatment. **b** The designed commercial product and its construction. **c** Working principle of the thermoelectric refrigeration system. **d** Infrared images of the hot and

cold sides of the cooling module. **e** Schematic overview of the strain-insensitive thermal sensor via a laminated strategy and spraying Fe(II) for the bonding of the adjacent layers, as well as the interfacial bridging structure. **f** Finite element analysis of the strain-insensitive mechanism.

numerous hydrogen bonds between MXene and CNF. The XPS analyses highlight synergistic effects, including hydrogen bonding, coordination bonding, and ionic bonding among CNF, MXene, and Fe(II), contributing to strong interfacial bridging in the composite (Fig. 2i). Furthermore, the Thermogravimetric-Differential Scanning Calorimetry (TG-DSC) experimental results further verify the strong interfacial bridging effect (Supplementary Fig. 8). The TG-DSC results reveal that the incorporation of Fe(II) reduces the total mass loss by 9.4% (from 57.37% to 47.95%) and increases the residual content to 52%, indicating enhanced thermal stability due to  $\text{Fe}^{2+}$  and carboxyl coordination. The small endothermic peak near 300 °C is attributed to the breaking of Fe-O coordination bonds, which is consistent with the FTIR data showing a shift of the -COOH vibration peak ( $1608 \text{ cm}^{-1}$ ).

To further explore the strain insensitivity and conductivity of the composite, we performed strain sensitivity tests. We observed that increasing the number of layers decreases strain sensitivity (Fig. 2j). Under increasing compressive stress, the film thickness decreases, leading to an initial gradual decline in resistance, followed by a sharp rise (Fig. 2k and Supplementary Figs. 9 and 10). Under tensile strain, the cross-sectional area decreases, resulting in tighter interlayer contact, but no obvious cracks on either the surface or the cross-section of the film under strains up to 50% are observed (Supplementary Fig. 11). This behavior is attributed to the interlocking and collaborative effects among CNF, PVA, MXene, and Fe(II) within the layered film structure. When external pressure is applied, the adjacent layers are forced closer together, creating new electron flow paths.



Conversely, more layers increase tensile strength, as the interlocking and presence of multiple layers enable the redistribution of stress within the structure, reducing the impact of localized strains. In practical applications, the thermal sensor thickness is influenced by both the number of layers and compression stress. A greater number of layers increases thickness, leading to higher strain insensitivity but lower elasticity. Excessive compression stress can cause damage, reducing temperature sensitivity, while insufficient compression stress hinders crosslinking. Therefore, balancing these factors is essential for optimal sensor performance.

and MXene composites. **i** Illustration of interfacial bridging based on synergistic effects between PVA, CNF, MXene, and Fe(II). **j**  $\Delta R/R_0$  versus strain for different layers stacking. **k** Resistance and thickness of PCMF as functions of the compressive stress for the laminated strategy.

The relationship between pressure, film thickness, intrinsic resistance, and strain insensitivity depends on the interaction mechanisms between the material components. As the film thickness decreases under excessive pressure, the conductive pathways may be disrupted or reorganized, increasing intrinsic resistance. Considering these factors, we chose 8 structural layers to achieve a skin-like stiffness ( $\sim 0.25$  MPa) and maintain temperature measurement stability during a 20 MPa compressive load, allowing the temperature-sensing layer to conform to human skin. Our results indicate that the strong interfacial bridging facilitated by Fe(II)

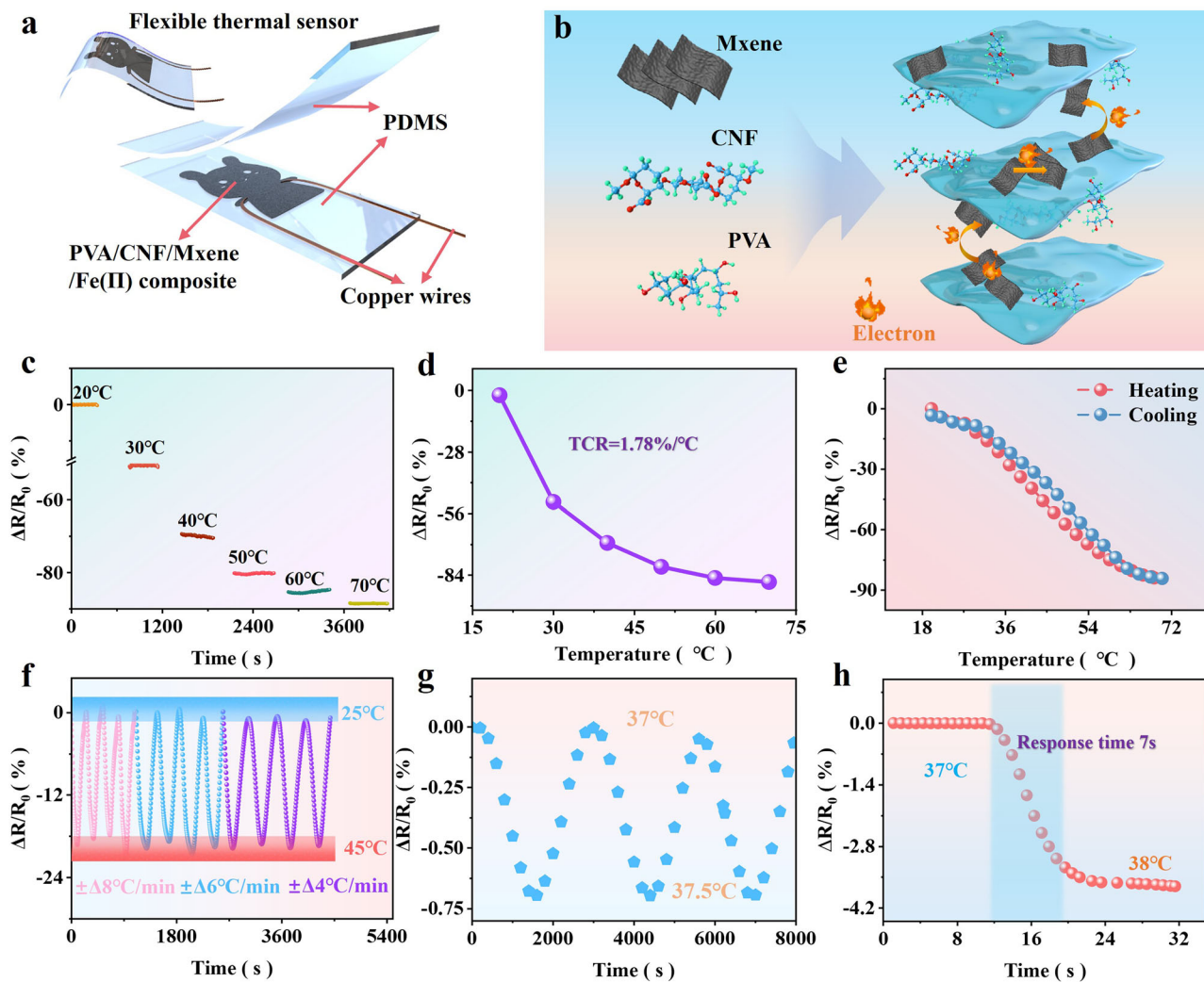


**Fig. 3 | Thermosensitive performances of the temperature module.** **a** Flexible thermal sensor. **b** Thermal sensing mechanism. **c** Negative resistance response to gradient temperature. **d** Heating and cooling cycles (20–70 °C). **e** Non-linear dependence of  $\Delta R/R_0$  versus temperature. Dynamic heating-cooling cycles of the

thermal sensor in **f** wide temperature range (25–45 °C, with temperature loading rates of 8 °C/min, 6 °C/min, 4 °C/min) and **g** temperature resolution 0.5 °C.

**h** Response time to temperature variation from 37 °C to 38 °C.

coordination and the synergistic interactions among CNF, PVA, and MXene enhance the strain-insensitive temperature sensing capabilities of the composite patch.

#### The laminated MXene-based flexible thermal sensor exhibits high thermosensitivity and rapid response suitable for human body temperature monitoring

To develop a flexible thermal sensor suitable for continuous body temperature monitoring, we constructed a device composed of three primary components: the thermal sensor element, PDMS encapsulation, and copper wires (Fig. 3a). The PDMS encapsulation protects the MXene material from environmental instability and prevents dust accumulation, thereby enhancing the sensor's durability. Copper wires serve as conduits for electrical connections between the sensor and the measurement or control system, enabling seamless data transmission. To achieve high thermosensitivity, we designed the thermosensitive mechanism of the alternating laminated composites based on their unique layered structure and the interactions between these layers (Fig. 3b). MXene nanosheets, functioning as the thermosensitive material, are uniformly dispersed within the polymer matrix, forming a highly conductive network. At elevated temperatures, the conductivity of MXene increases due to the activation of additional electrons from the valence state to the conduction state.

To evaluate the thermal responsiveness of the flexible sensor, we measured changes in electrical resistance ( $\Delta R/R_0$ ) as a function of temperature variation. We observe that the resistance of the sensor consistently decreases in a nonlinear manner within the thermal condition spanning from 20 °C up to 70 °C (Fig. 3c), including a range suitable for human health monitoring. This behavior confirms the negative temperature coefficient (NTC) characteristic of MXene, underscoring its efficacy as a thermosensitive material. To quantify the thermosensitive performance, we employ the temperature coefficient of resistance (TCR):

$$\text{TCR} = (R_2 - R_1)/(R_1 \times \Delta T) \quad (1)$$

where  $R_2$  and  $R_1$  represent the resistance at higher and lower temperatures, respectively, and  $\Delta T$  denotes the temperature difference between the two measurements. A higher TCR indicates greater thermosensitivity. We find that the TCR exhibits a nonlinear variation, dramatically increasing from  $0.2\text{ }^{\circ}\text{C}^{-1}$  to  $4.8\text{ }^{\circ}\text{C}^{-1}$  across the temperature range of 20–70 °C (Fig. 3d). The average TCR of  $1.78\text{ }^{\circ}\text{C}^{-1}$  greatly surpasses literature values for temperature-sensitive patches. To assess the sensor's stability and durability, we performed cyclic heating and cooling tests between 20 °C and 70 °C. We observed consistent thermal responses with overlapping curves and negligible hysteresis (Fig. 3e). We further verified the sensor's performance

under different temperature cycles with varying loading rates ( $\pm 4\text{ }^{\circ}\text{C min}^{-1}$ ,  $\pm 6\text{ }^{\circ}\text{C min}^{-1}$ ,  $\pm 8\text{ }^{\circ}\text{C min}^{-1}$ , as shown in Fig. 3f) and temperature ranges (25–35 °C, 25–45 °C, 25–50 °C in Supplementary Fig. 12). We found that the sensor withstands a maximum loading rate of 8 °C/min and 20 alternating cycles without noticeable signal fluctuation, maintaining a TCR of 1.35–2.2% °C<sup>-1</sup>. These results indicate that the sensor performs well under demanding conditions.

To evaluate the sensor's responsiveness within the human body temperature range, we test its temperature resolution and response time. We observed that the sensor achieves a desirable temperature resolution of 0.5 °C (Fig. 3g), enabling precise monitoring. The resistance change is 0.75%, which is comparable to the resistance change under 5% strain, and at this strain, it does not significantly affect the accuracy of temperature measurement. Furthermore, we found that the sensor demonstrates an exceptional instantaneous response time of approximately 7 seconds when subjected to a temperature change from 37 °C to 38 °C (Fig. 3h), reinforcing its potential for real-time applications. Considering that the temperature coefficient of resistance (TCR) is 2% °C<sup>-1</sup> within the range of 30–40 °C, if no resistance change compensation is applied, the allowable resistance variation for a 1 °C accuracy loss is 2%. The resistance change reaches approximately 2% by the fourth day, indicating that the sensor can maintain its performance stability for at least 4 days (Supplementary Fig. 13). The observed variation in resistance, which exceeds 10% after approximately eight days, indicates potential limitations in the long-term stability of the material. The PDMS encapsulation layer permits the permeation of oxygen, thereby facilitating the oxidation of Fe(II) to Fe(III), which increases the resistance of the MXene layer. The primary mechanism responsible for the long-term instability is the electrolytic reaction of FeCl<sub>2</sub> within the polymer matrix. With an average TCR of 1.78% °C<sup>-1</sup>, a 6% resistance increase from 16% strain could mimic a 3.4 °C temperature rise. However, under real-world infant monitoring during physiologically stable conditions with strain <5%, resistance changes remain minimal (<0.75%), keeping temperature error below 0.5 °C. For large strain applications, our 16-layer composite reduces 16% strain effects to a 0.46% resistance change (GF = 0.08), optimally balancing comfort, strain insensitivity, and thermal accuracy for pediatric care.

In summary, our flexible thermal sensor exhibits superior thermosensitivity (1.35–2.2% °C<sup>-1</sup>), reliable operation across a wide temperature range (20–70 °C), stability during alternating temperature cycles (20 cycles), rapid response time (~7 s), and high-temperature resolution (0.5 °C). These features are attributed to the incorporation of thermosensitive MXene nanosheets and the innovative laminated design, which collectively outperform conventional systems using nanoparticles or nanofillers such as carbon nanotubes (CNTs), graphene, silver (Ag) wires, and Platinum (Supplementary Fig. 14 and Supplementary Table 1). The results indicate that our sensor holds significant potential for human body temperature monitoring in wearable biomedical devices.

### Laminated structure and interlocking mechanism enable strain-insensitive thermal sensing

While our previous studies confirm the accuracy and reliability of the flexible thermal sensor in static conditions, achieving precise thermosensing in dynamic environments requires addressing strain sensitivity. To this end, we investigated how the sensor's innovative design, featuring alternating laminated layers and interfacial interlocking, contributes to strain-insensitive thermal sensing.

To assess the strain-insensitive characteristics of the sensor, we performed both experimental and theoretical analyses. Experimentally, the surface topography of the composites was obtained using confocal laser scanning microscopy (CLSM). The analysis revealed that the surface of primitive polyvinyl alcohol (PVA) is smooth (Fig. 4a). In contrast, the PVA/CNF, PVA/CNF/MXene, and PVA/CNF/MXene/Fe(II) composites exhibit significant protrusions and increased roughness values ranging from 1.7 to 4.7. These rough microstructures enhance surface contact and expose more

hydrophilic groups (−OH, −COOH), leading to stronger interfacial bonds driven by the collaborative effects among PVA, CNF, MXene, and Fe(II). The results indicate that the laminated structure contributes to strain insensitivity under dynamic conditions.

Theoretically, we investigated the strain insensitivity characteristics of the tough surface and alternating laminated architecture using FEA (Fig. 4b)<sup>41,42</sup>. We simulated the stress–strain evolution under sensing layer deformations ranging from 7% to 31.1%. We observed that significant stress distribution occurs beneath the interlocking regions of adjacent layers, as indicated by brightly colored areas in the simulation results. These regions provide numerous pathways for stress transfer, amplified by enlarged contact areas. Furthermore, its strain-resistance performance is notable, with a gauge factor of 0.5 within the 0–30% strain range (Supplementary Fig. 15). This value is substantially lower than that of homogeneous composites (GF > 0.7). The mechanism relies on dynamic chemical interactions among components. Fe(II) ions serve as hooks, establishing strong coordination bonds between CNF and MXene, while PVA chains form a stretchy hydrogen-bonded network. These interactions distribute external stress like a car's shock absorber, preventing localized stress buildup that leads to cracking. The highest principal stress at the interlocking interfaces induces for sliding and bending at the interfaces, rather than cracking, resulting in in-plane stress dispersion near the contact elements (Supplementary Fig. 16). The results indicate that the combination of strong interfacial interlocking and rough textured surfaces suppresses deformation and minimizes interfacial interactions, thereby enabling strain-insensitive thermosensation.

To further evaluate strain insensitivity, we integrated classical mechanics with experimental validation. Using classical lamination theory (CLT), we modelled interlayer stress distribution in the laminate structure, where rigid MXene/PVA ("bricks") and flexible CNF/Fe(II) ("mortar") layers enable uniform stress propagation. The interlocking architecture enhances interfacial contact area for optimized load transfer, preventing early interface failure. CLT shows that increasing layers improves stress transfer efficiency, reducing strain sensitivity (Fig. 2k). Micromechanical analysis via the rule of mixtures calculates the laminate's effective elastic modulus, confirming that a higher ratio of rigid MXene/PVA layers lowers the gauge factor (GF), aligning with reduced strain sensitivity (Fig. 2j). FEA simulations (Fig. 4b) validate stress concentration in interlocking regions, facilitating stress dissipation through micro-sliding/bending rather than cracking. Experimentally, under infant movements (strain <5%), resistance change remains <0.75%, leading to a 0.5 °C temperature error (Fig. 3g). The laminate structure decreases mechanical noise, ensuring resistance variations primarily reflect thermal signals.

To validate the numerical simulation results, we conducted experimental comparisons. We observed that the laminated structure with efficient interfacial locking exhibits superior strain-insensitive thermosensing capabilities compared to structures lacking this feature (Fig. 4c). This enhanced performance is attributed to the PVA/CNF/MXene/Fe(II) composite's ability to effectively absorb stress in a vertical stress field, thereby limiting deformation and reducing strain sensitivity, as illustrated in Fig. 4d. To assess the mechanical robustness of the composites, we performed puncture resistance tests. We found that the PVA/CNF/MXene/Fe(II) and PVA/CNF/Fe(II) composites exhibit significantly greater puncture resistance than the PVA/CNF and PVA/CNF/MXene counterparts (Fig. 4e). This indicates that the inclusion of Fe(II) enhances mechanical strength. We also evaluate the temperature response of both punctured and non-punctured flexible thermal sensors and observe similar responses ( $\Delta R/R_0 \sim -50\%$ ,  $\Delta T \sim 20\text{ }^{\circ}\text{C}$ ), highlighting negligible hysteresis (Fig. 4f). This suggests that the sensor maintains its thermosensing performance even after mechanical damage. Furthermore, we conducted cyclic fatigue testing under 30% strain, while the material retained 92% of its electrical stability after approximately 8,000 cycles (Supplementary Fig. 17), indicating excellent durability. The loading–unloading curves exhibit larger hysteresis and residual strains for composites with Fe(II) (Fig. 4g,h), suggesting enhanced energy dissipation mechanisms due to the presence of Fe(II). Cross-

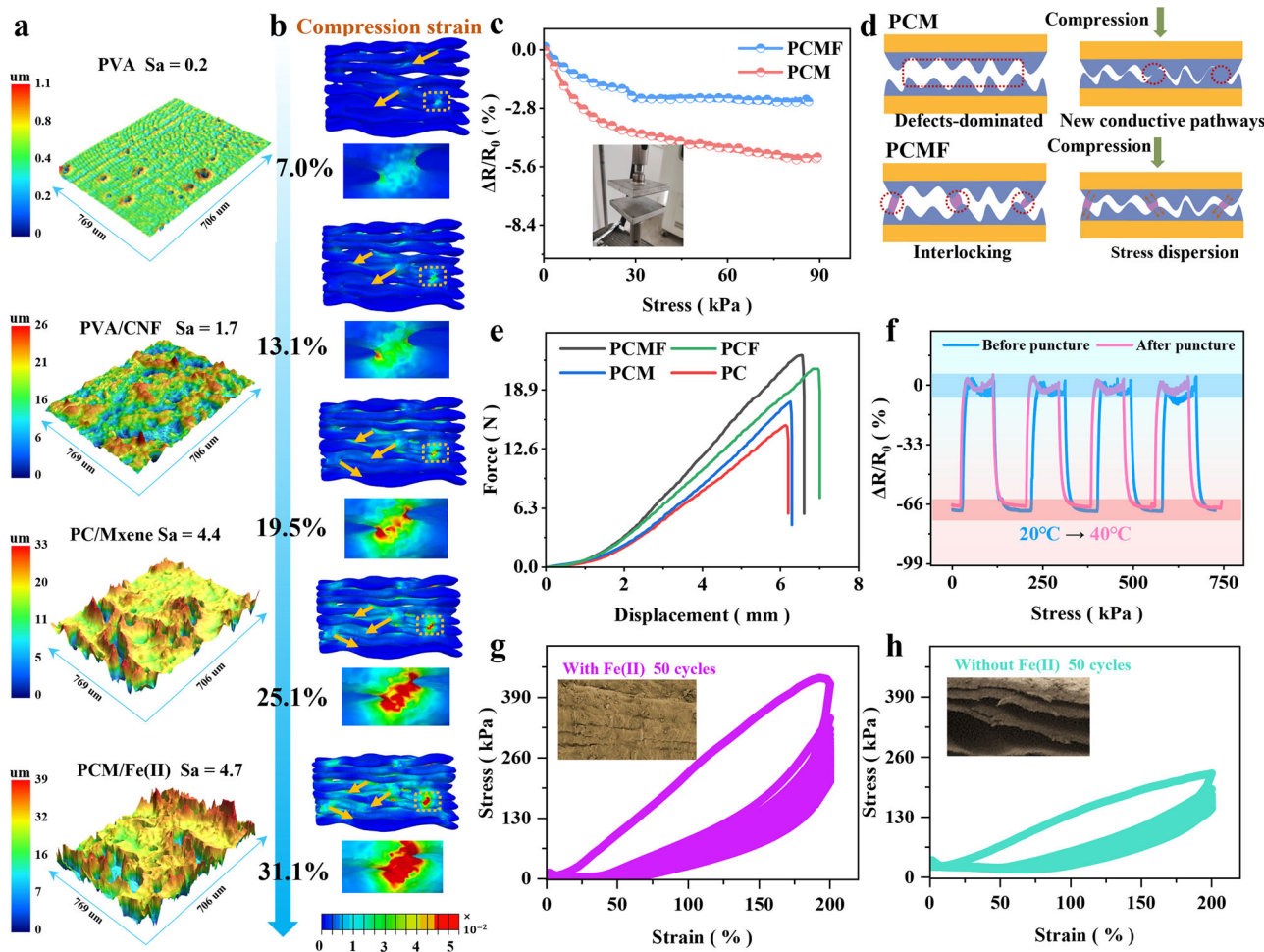


**Fig. 4 | Strain-insensitive thermal sensor via laminated structure and interlocked effect.** **a** Confocal laser scanning microscope (CLSM) images reveal the surface roughness of the interfacial bridging. **b** Finite element analysis of stress distribution of laminated architecture at varying deformation ratios (7.0%, 13.1%, 19.5%, 25.1%, 31.1%). Strain-insensitive **(c)** test and **(d)** mechanism. **e** Puncture test for PVA/CNF/

MXene/Fe(II) composites (PCMF), PVA/CNF/MXene composites (PCM), PVA/CNF/CNF composites (PCF) and PVA/CNF composites (PC). **f** Thermosensitivity maintenance of thermal sensor with strain-insensitivity after being punctured. Cyclic loading and unloading curves for PCMF **(g)** and PCM **(h)**. Insets show cross-sectional SEM images after 50 cycles.

sectional SEM images confirm the robust profiles resulting from the laminated structure and effective interfacial bridging.

In practical applications, the thickness of PDMS encapsulation significantly impacts the strain-insensitivity behavior of the sensor. As the encapsulation thickness increases from 0.6 mm to 1.4 mm, both axial and vertical strain decrease (10.2% and 15.5%, respectively) due to enhanced mechanical damping (Supplementary Fig. 18). This leads to a reduction in the piezoresistive response, with an 18% decrease in resistance variation for the thicker encapsulation (1.4 mm) compared to the thinner one (0.6 mm). While thicker encapsulations reduce strain effects and improve sensor stability, they introduce a temperature gradient due to the insulating properties of PDMS, which can affect temperature measurements by increasing thermal resistance. To balance these factors, a 400  $\mu$ m thick PDMS encapsulation is used in this study. A 2 mm thick PDMS block (2 cm  $\times$  2 cm) is also added between the thermal sensor and FPCB to maintain consistency in mechanical properties and ensure the combined thickness matches that of the thermoelectric cooler. Additionally, under typical infant forehead movements (strain  $<5\%$ ), the resistance change is  $<0.75\%$ . This corresponds to a temperature error of 0.5  $^{\circ}$ C, which is within the sensor's resolution (Fig. 3g). Under typical infant forehead movements ( $<5\%$  strain), the resistance change is  $<0.75\%$ , equivalent to a 0.5  $^{\circ}$ C temperature error (within the sensor's resolution).

These results indicate that the laminated structure and interlocking mechanism significantly enhance the strain-insensitive thermal sensing

capabilities of the sensor, making it suitable for dynamic wearable applications.

#### Optimizing electrical parameters enhances the cooling performance of the thermoelectric module for in-situ temperature regulation

To enable active regulation of abnormal body temperatures, we integrated the flexible thermal sensor with a thermoelectric cooling module, creating a comprehensive closed-loop system for managing body temperature. To evaluate the performance of the cooling module, we designed an experimental setup (Fig. 5a) that includes a heater to simulate heat generation, a voltage source to power the thermoelectric cooler, a thermocouple thermometer for real-time temperature measurement, and a PDMS film to simulate human skin's heat transfer properties. The thermoelectric cooling module consists of two different semiconductor materials, electrically connected in series and thermally in parallel, generating a temperature difference for efficient cooling or heating (Fig. 5b). By controlling the current flow, we can actively cool or heat specific areas (Fig. 5c).

To investigate the effect of the cooling module's electrical resistance on the cold-side temperature and coefficient of performance (COP), we studied its performance under various thermal resistive conditions (Supplementary Fig. 19). We observed that, in both low and high thermal resistance scenarios, cooling modules with higher electrical conductivity achieve superior cooling effects, attaining lower cold-side temperatures (Fig. 5d, e). The

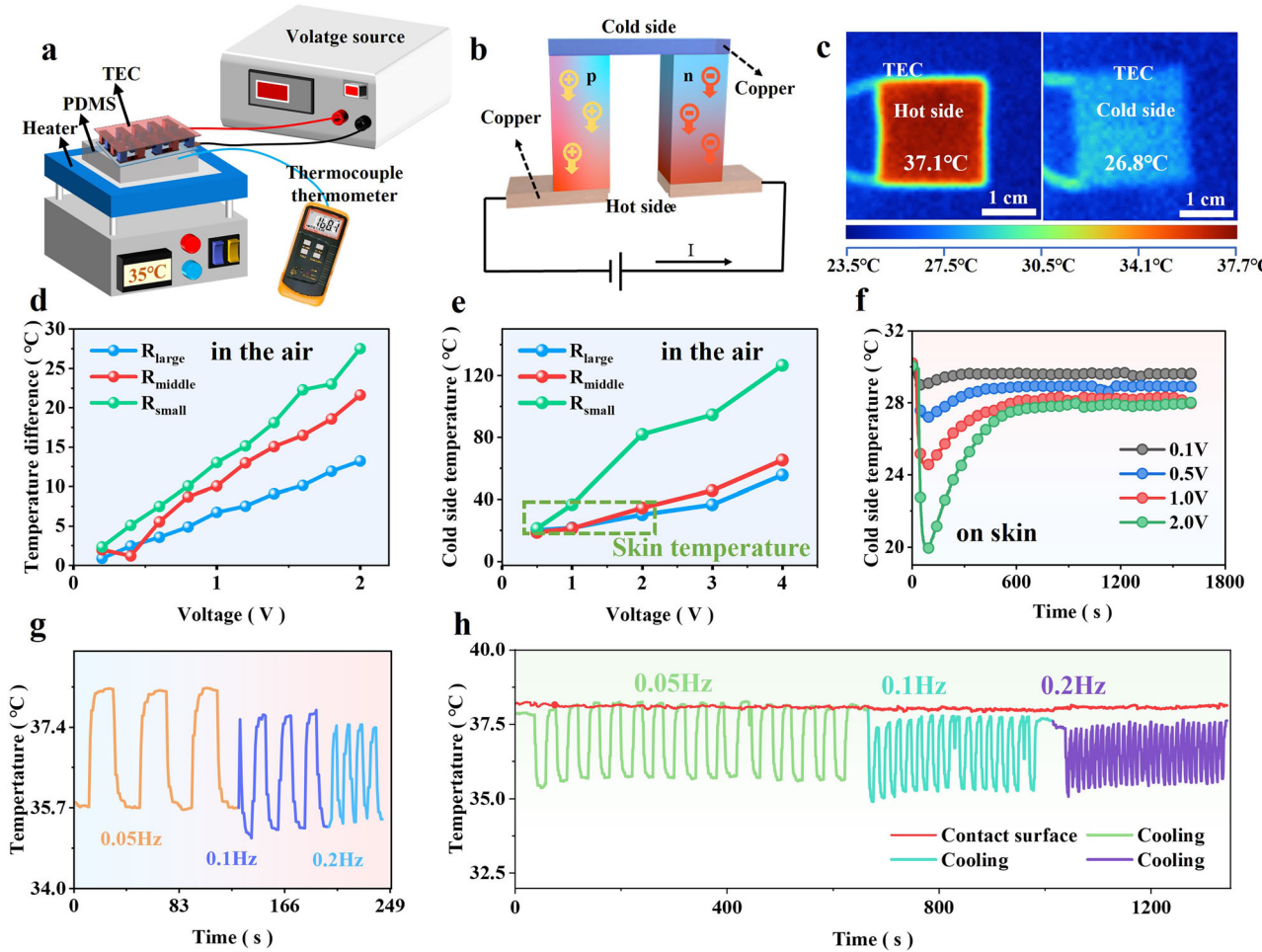


**Fig. 5 | In-situ cooling treatment of the thermoelectric cooling module.**

a Schematic of an experimental setup to simulate fever for assessing performance of the thermoelectric cooling module. b Schematic representation of thermoelectric cooling mechanism. c Infrared thermal imaging diagram of thermoelectric module for personal in-situ cooling treatment. d The final stabilization temperature of the cold side in thermoelectric modules and e temperature difference between two sides

(with resistors resistance of the thermoelectric cooling module = of  $1.7\ \Omega$ ,  $2.4\ \Omega$ , and  $6.0\ \Omega$ ) under different voltages while both cold and hot sides exposed to the surrounding air. Cooling effects at different f voltages (0.1 V, 0.5 V, 1 V, 2 V, on skin) and g frequencies (0.05 Hz, 0.1 Hz, 0.2 Hz at 1 V). h The stabilization and repeatability of cooling effect.

results indicate that enhanced electrical conductivity facilitates better current flow, thereby boosting cooling performance. However, we also found that increasing the voltage improves the cooling temperature difference but raises the current, which can generate additional heat due to self-resistance. This self-heating effect may cause the cold-side temperature to rise above ambient levels if not properly managed (Supplementary Fig. 20). Additionally, the thickness of the packaging results in a lower cooling rate, and the more time required to reach the stabilized temperature increases (Supplementary Fig. 21). Therefore, effective heat dissipation on the heat source side is crucial for maintaining cooling efficiency on the heat sink side (Supplementary Fig. 22). As shown in Fig. 5f, increasing the voltage initially lowers the cold-side temperature but can later cause it to rise due to heat transfer from the heat source side. Despite this, the cooling response remains effective, maintaining the final temperature below the initial skin temperature.

To understand the effect of applied voltage frequency on the thermoelectric cooling module, we investigated its cooling performance at different frequencies (0.05 Hz, 0.1 Hz, 0.2 Hz). We observed that higher frequencies generally result in better cooling effects (Fig. 5g), and cyclic stability is demonstrated due to thermal inertia and response time (Fig. 5h). At lower frequencies, such as 0.05 Hz with a 20-s “on” and “off” cycle, the module has a longer “on” phase, allowing for a greater transient temperature difference. During the “off” phase, more heat transfers from the thermal

source side to the heat dissipation side, resulting in a smaller final stable temperature. In contrast, at higher frequencies like 0.2 Hz, the module has less “on” time, leading to a lower temperature difference but a lower final stable temperature, 3 °C below ambient. This sacrifices a larger temperature difference for a lower stable temperature. We found that at very high frequencies, the module may not fully respond to each voltage cycle, limiting the maximum cooling potential. As frequency increases, the on-off periods shorten, restricting heat transfer from the thermal source side to the heat dissipation side. Consequently, the cold-side temperature drops below the initial ambient temperature. The results indicate that selecting an optimal frequency that balances cooling efficiency and temperature differentials, considering thermal characteristics, is crucial.

#### Integrated wearable system provides continuous temperature monitoring and effective in-situ cooling for infant care

To create a comprehensive system for temperature perception and in-situ cooling, we integrated the flexible thermal sensor with the thermoelectric cooling module. We developed a wearable device capable of monitoring different body parts such as the mouth, forehead, armpit, chest, and wrist (Fig. 6a and Supplementary Movie 2). The device consists of key layers, each with a specific role. The Flexible Substrate Layers protect the internal circuits and sensors from dust and contamination. The FPCB Layer handles electrical connections and signal transmission. The Thermal Sensor Layer

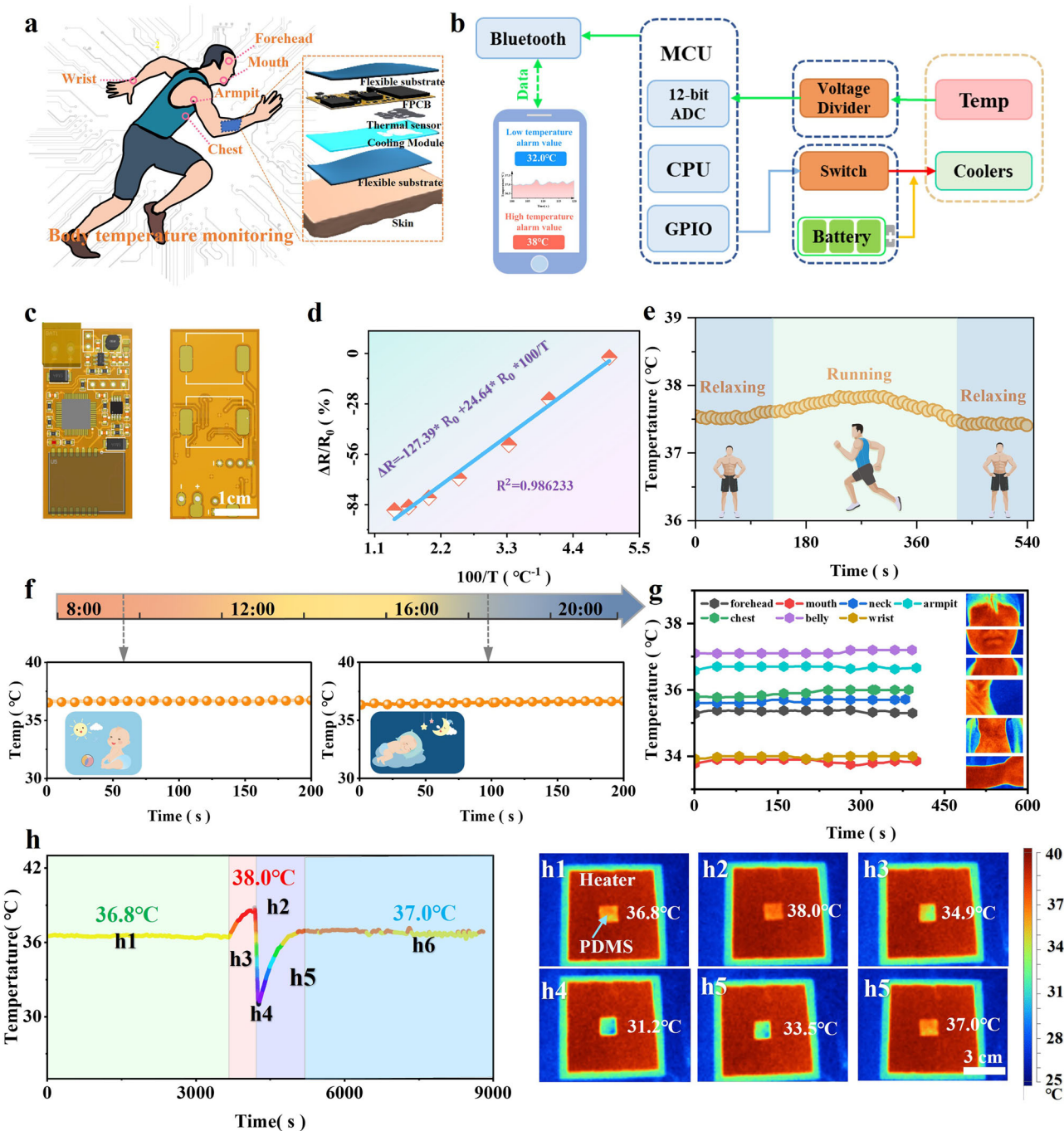


**Fig. 6 | Assessments of the smart temperature patch in both static and dynamic scenarios for personal thermoregulation.** **a** An overview of body temperature monitoring. **b** Schematic diagram of the functional modulus of the smart temperature patch. **c** FPCB of the smart temperature patch for signal transmission and procession. **d** The relationship between resistance and temperature. **e** Real-time

temperature detection during relaxing and running. **f** Infant's temperature detection in the morning and evening. **g** Real-time and accurate temperature detection with stability across different parts of body. **h** Personal thermoregulation test, including fever detection and in-situ cooling treatment.

monitors temperature, tracking body temperature to ensure safe operation. The Cooling Module Layer prevents overheating, maintaining optimal temperatures for stability. Lastly, the Skin Layer simulates human skin. This system detects temperature deviations, helping identify potential health issues like fever or infections.

We constructed the wearable system to facilitate dynamic and continuous temperature monitoring through the flexible thermal sensor. The sensor transmits data in real-time to a mobile application via Bluetooth, with a display resolution of  $0.05^{\circ}\text{C}$ . When the temperature of the targeted region exceeds the normal human body range, the microcontroller unit (MCU)

activates the thermoelectric cooling module to regulate the temperature (Fig. 6b). This closed-loop system ensures efficient and timely temperature management, enhancing both health monitoring and comfort.

We designed the control circuit board with four key components, as illustrated in Fig. 6c and Supplementary Fig. 23. The first component is the temperature sensor interface, which supports multiple sensor connections, although only one is used in our experiment. The second component is the temperature processing and control unit, which processes temperature data, performs calculations, and makes decisions based on variations of relative resistance with temperature (Fig. 6d). The third component is the

thermoelectric cooling module, positioned underneath the control circuit board, providing localized cooling therapy upon activation by the MCU. The fourth component is the power supply management system, featuring circuitry for lithium battery operation, regulating and distributing power to the system components. The thermal sensor and thermoelectric cooler are mounted underneath the FPCB, each occupying approximately half of the available space. The thickness of the temperature sensor is carefully matched with the thickness of the thermoelectric module to maintain uniformity. This design ensures that the device does not interfere with wearability, providing comfort during use without causing any noticeable discomfort (Supplementary Fig. 24).

We test the system's capability to provide continuous and precise temperature monitoring under dynamic conditions. We observed that the device functions effectively during physical activities such as running (Fig. 6e), during early morning and evening monitoring of children (Fig. 6f), and when measuring temperature on different body parts (Fig. 6g). Upon detecting abnormalities, thermoelectric cooling technology is activated for targeted cooling.

To demonstrate the module's capability for localized cooling, we conducted a simulated experiment (Fig. 6h). We used a PDMS film representing skin, which we heated to mimic prolonged fever, raising the temperature from 36.8 °C to 38 °C and maintaining it at this level for approximately 2 min. We then activated the thermoelectric cooling module, which rapidly decreased the PDMS film temperature to 31.2 °C before it slowly increased and stabilized at 37.0 °C. We observed that the module effectively reduces the temperature, indicating its potential for fever reduction or temperature management applications. The results indicate that the integrated wearable system provides continuous temperature monitoring and effective in-situ cooling, making it a promising tool for infant care and other biomedical applications requiring precise temperature control.

The potential applications of this wearable system are vast. In addition to infant care, it could be beneficial in sports, as demonstrated in Fig. 6e, where the device effectively monitors body temperature during physical activities like running, helping athletes manage their temperature during exercise and prevent heat-related illnesses. Furthermore, the system could be used for burn treatments by providing targeted cooling to affected areas, offering a non-invasive method to mitigate pain and limit tissue damage<sup>8,27,46</sup>. These applications underscore the system's versatility, extending its use beyond just health monitoring to areas like sports and burn management.

## Discussion

In this study, we have developed a novel wearable device that integrates a strain-insensitive thermal sensor with a thermoelectric cooling module, aiming to enhance infant care through continuous temperature monitoring and in-situ cooling treatment. Wearable temperature sensors often face challenges related to strain sensitivity caused by body movements, which can lead to inaccurate readings and unreliable monitoring<sup>41,42,53,54</sup>. Overcoming this limitation is crucial for ensuring precise and continuous health monitoring in dynamic environments. To address this issue, we engineered a thermal sensor employing an alternating laminated architecture with interfacial interlocking. This design effectively minimizes strain-induced resistance changes by dispersing stress and preventing layer slippage, achieving a remarkable strain insensitivity with a gauge factor of 0.5. The interlocking mechanism ensures that mechanical deformations do not significantly affect the electrical conductivity, thereby maintaining the accuracy of temperature measurements even under motion<sup>55–58</sup>. The incorporation of MXene nanosheets, known for their high electrical conductivity and mechanical flexibility, further enhances the sensor's performance<sup>59,60</sup>. By integrating MXene with PVA and CNF, and introducing Fe(II) ions as crosslinking agents, we established strong interfacial interactions through hydrogen bonding and coordination bonds. This synergistic combination contributes to the sensor's high thermosensitivity and mechanical robustness. Recent studies have explored various strategies

to achieve strain-insensitive sensing. For instance, a crack-based sensor was developed to minimize strain effects<sup>42</sup>, while serpentine structures were utilized to accommodate mechanical deformations<sup>61</sup>. Compared to these approaches, our laminated interlocking design offers a simpler fabrication process and better integration with flexible substrates, making it more suitable for practical applications in wearable devices.

Active temperature regulation in wearable devices presents a significant advancement in personalized healthcare, allowing not only monitoring but also immediate intervention<sup>62</sup>. By integrating a thermoelectric cooling module into our wearable device, we provide a means for in-situ cooling treatment upon fever detection. This module effectively lowers skin temperature by up to 2 °C, with a cooling rate of 1 °C per hour and a coefficient of performance up to 0.6, ensuring timely interventions and enhancing infant comfort. The thermoelectric cooling module operates based on the Peltier effect, enabling precise control of the cooling process without moving parts or refrigerants<sup>45</sup>. This integration allows for rapid temperature reduction on the skin surface, enhancing comfort and potentially preventing febrile seizures in infants<sup>63</sup>. Previous research has investigated various cooling methods in wearable systems. For example, a flexible thermoelectric generator was developed for body heat harvesting<sup>64</sup>, and a wearable microfluidic system was developed for sweat-based cooling<sup>65</sup>. Our approach distinguishes itself by focusing on active cooling rather than passive heat management, providing immediate and controllable temperature regulation.

The combination of strain-insensitive sensing and active cooling addresses critical needs in infant care. Infants are particularly vulnerable to rapid temperature changes, and timely intervention is essential for their health<sup>66</sup>. Our device enables caregivers to continuously monitor an infant's temperature with high accuracy and respond promptly to fevers by activating the cooling module. This technology has the potential to reduce the burden on caregivers by providing an automated system that alerts and initiates cooling without constant supervision. Moreover, the data collected can offer valuable insights into an infant's health patterns, aiding in early diagnosis and treatment. Beyond infant care, the principles and design of our wearable device can be extended to other biomedical applications requiring precise temperature monitoring and regulation. For instance, managing hyperthermia in athletes<sup>67</sup>, monitoring wound healing processes<sup>68,69</sup>, or even temperature-sensitive drug delivery systems<sup>70</sup>.

While our study presents significant advancements, there are limitations and challenges that need to be addressed in future research. (1) Scalability and manufacturing: scaling up the production of the laminated interlocking sensor with consistent quality could present challenges. Advanced manufacturing techniques, such as roll-to-roll processing, may be explored to enhance scalability<sup>71</sup>. (2) Long-term stability and biocompatibility: the long-term stability of MXene materials in physiological conditions needs thorough investigation. Encapsulation strategies and biocompatibility assessments are essential to ensure safety for prolonged skin contact<sup>72</sup>. (3) Power efficiency: the thermoelectric cooling module requires a power source, which may limit the device's portability and usage time. Developing energy-efficient components or integrating energy-harvesting technologies could mitigate this issue<sup>73–75</sup>. (4) Miniaturization and intelligence: Integrating an advanced SoC chip, reducing component density to enhance portability and lightness, and a large language model for health guidance<sup>76</sup>. (5) Regulatory and clinical translation: Navigating regulatory pathways and conducting clinical trials will be necessary steps toward commercializing this technology. Collaboration with healthcare professionals can facilitate this process<sup>77</sup>.

Our study introduces a novel wearable device that combines strain-insensitive temperature sensing with active thermoelectric cooling, offering a comprehensive solution for infant care. The innovative design addresses key challenges in wearable biomedical devices, and the integration of active cooling represents a significant advancement in personalized healthcare. Future work will focus on optimizing the device for real-world applications and exploring its potential across various biomedical fields.

## Methods

### Preparation of materials

The single-layer  $Ti_3C_2T_x$  (MXene) solution (20 mg/ml) was obtained from Xinx Technology Company. Cellulose nanofibril suspensions (CNF, 1.34%, a length ranging from 400–1000 nm, and a diameter of 5–10 nm) were purchased from Tianjin Mujingling Biotechnology Company. Poly(vinyl alcohol) (PVA,  $M_w = 205,000\text{ g mol}^{-1}$  and a degree of hydrolysis of 87.0–89.0%), sodium hydroxide (NaOH), and iron (II) chloride tetrahydrate ( $FeCl_2 \cdot 4H_2O$ ) were acquired from Xi'an Haotian Glass Instrument Company. Polydimethylsiloxane (PDMS) was also included from Xi'an Haotian, with a weight ratio of 1:10, as used throughout the manuscript.

### Fabrication of thermal sensor with multi-layer interlocking architecture

The detailed fabrication process is as follows (Supplementary Fig. 1): PVA powder (0.23 g) and CNF suspensions (0.2 g) were dissolved in deionized water (2.85 g) at 90 °C using magnetic mixing (800 rpm, 2 h) for a homogeneous mixture (3.0 g). After the mixture reached room temperature, MXene (3 ml) was added to the above mixture, an ultrasound was performed for 1 h under an argon environment, and then centrifuged the mixture to remove residual bubbles. Next, PVA/CNF/MXene composite (PCM) films were fabricated by using a blade coating machine (50 mm  $min^{-1}$ ), followed by a drying process for 24 h at 30 °C. The dried composite films were soaked in a highly concentrated alkaline hydroxide (6 M, 1 L) for 25 min to enhance PVA crystallinity (Supplementary Fig. 2), and then washed with deionized water. After drying, Fe(II) solution (1 M) was sprayed to obtain PVA/CNF/MXene/Fe composite (PCMF) film. The resulting multilayered PCMF was formed through compression by using a Bose fatigue testing machine (20 MPa, 20 min) and subsequently encapsulated by using a plastic sealing film.

### Architecture characterizations

Scanning electron microscopy (SEM) observation and energy dispersive spectroscopy (EDS) were conducted by a field emission scanning electron microscope (Verios G4, FEI). Transmission electron microscopy (TEM) photographs were captured using a FEI Talos F200X TEM to observe the cross-linked components. Morphological observations were performed by a light microscope (BX43, Olympus). Laser confocal microscopy (LEXT OLS4000, Olympus) was used to observe the composites' average surface roughness and 3D profile. XRD diffraction images were measured on a D8 DISCOVER A25 equipped with Co radiation to examine the crystallinity of sodium hydroxide. X-ray photoelectron spectroscopy (XPS, ESCALAB 250XI, Thermo Scientific) was used to evaluate interfacial cross-linking. Fourier transform infrared spectroscopy (FTIR, Tensor II, Bruker) was conducted at room temperature over a range of 400–4000  $cm^{-1}$ . The atomic force microscope (AFM) (Bruker Multimode 8) was used to observe surface roughness. The thermogravimetric-differential scanning calorimetry (TG-DSC) (STA 449 F3 Jupiter) was used for thermal property analysis of the thermal sensor.

### Evaluation of mechanical properties and thermal sensitivity

Uniaxial tensile and fatigue cycle tests were performed on the multi-layer thermal sensor by using an INSTRON 3344 material mechanics testing machine. The resistance change of the thermal sensor was simultaneously measured by a Keithley 2450 digital source meter. Stress relaxation tests were conducted by using a BOSE Electroforce 3330 fatigue tester with 150 N loading. Temperature loading was achieved by a Rapid variable temperature experiment box (TAR-63L). Real-time temperature detection was recorded by using a multichannel thermometer (K-type thermocouple, YET-610) and an infrared (IR) camera (ST9450).

### Finite element analysis

Strain-insensitivity: Finite element analysis (FEA) was conducted by using ABAQUS/CAE. In the simulation, a PVA/CNF/MXene/Fe(II) composite (PCMF) with cross-linking architecture between layers was modeled as a

linear elastic material. The basic material properties assigned to the model were Young's modulus ( $E$ ) = 360 kPa, Poisson's ratio ( $\nu$ ) = 0.3, and density ( $\rho$ ) = 1.35. The bottom surface of PCMF was set as a fixed boundary condition, while the top surface was subjected to displacement loading. The displacement loading in the z-direction was set to 50% of the thickness (0.6 mm). To vividly visualize the strain insensitivity, an interlayer interconnection architecture model was developed by using the CINEMA 4D R25 software. The interface between adjacent layers was created by expanding from a plane to a volume and introducing random noise to all planes. In order to ensure that the model can be imported into ABAQUS for calculation, the model needs to be repaired by using Geomagic Design X software. After repairing, it is then imported into HyperMesh for meshing, and finally imported into ABAQUS for FEA.

Effect of cover case thickness: The PDMS has an elastic modulus of 800 kPa, with dimensions of 4 cm  $\times$  2 cm and thicknesses of 0.6 mm, 1.0 mm, and 1.4 mm. The thermal sensor has dimensions of 3.5 cm  $\times$  1.5 cm  $\times$  0.3 mm and an elastic modulus of 360 kPa. The interface between the thermal sensor and PDMS is bonded. The applied tensile displacement is 1 cm.

### Strain-insensitivity assessment

The puncture strength tests were performed by using a Zwell/Roell universal material tester equipped with a sample fixing station that had a round hole of 30 mm diameter in the center. A steel needle with a 450  $\mu\text{m}$  radius was used for puncturing the sensor. The descending steel needle was loaded at a 50 mm  $min^{-1}$  rate to obtain the maximum loading force. Tensile tests were conducted by using a Bose Electroforce 3330 fatigue machine. Vertical force was applied to a square sample holder to fix the thermal sensor, and resistance change was measured by using a Keithley 2450 digital source meter to evaluate strain insensitivity:

$$GF = \frac{\Delta R / R_0}{\epsilon} \quad (2)$$

In the above equation,  $\Delta R$  is the resistance change,  $R_0$  is the initial resistance,  $\epsilon$  is tensile strain, and gauge factor (GF) is strain sensitivity. A lower value of GF corresponds to a higher degree of strain insensitivity.

### Thermoelectric cooling module

The thermoelectric cooling modules used in this study were fabricated utilizing commercial p-type and n-type bismuth telluride. Three different sizes were available: 20 mm  $\times$  20 mm  $\times$  2.2 mm, 23 mm  $\times$  23 mm  $\times$  2.1 mm, and 25 mm  $\times$  25 mm  $\times$  2.0 mm, each containing 49, 71, and 127 legs, respectively. These thermoelectric cooling modules were purchased from Guangzhou Mustache Electronics Technology Co. The resistance of the thermoelectric cooling modules varied, with values of 1.7, 2.4, and 6 ohms, respectively. For effective heat dissipation and absorption, both the heat sink and heat source sides of the thermoelectric cooling modules were made of copper. To simulate human fever cooling, a PDMS film was placed between the heater (DRB-3/3D) and the thermoelectric cooling module. All temperature measurements in the study were obtained by using a K-type thermocouple (YET-610). Cooling treatment was applied by supplying a current or voltage to the thermoelectric cooling modules with a Keithley 2450 digital source meter.

### Wireless electronic integrated system

A wireless electronic integrated system included a PCMF sensing module, a thermoelectric cooling module, and a flexible printed circuit board (FPCB) (Supplementary Fig. 23). FPCB consisted of three essential components: (1) a lithium battery ( $0.8 \times 0.8 \times 0.6\text{ mm}^3$ ) acting as the power supply for the system; (2) a Bluetooth module (HC-04) enabling wireless communication; (3) the circuit system incorporates the STM32F103C8T6, a 32-bit microcontroller (MCU) that acts as the central control unit. This MCU is equipped with digital input/output ports, 12-bit analog-to-digital converters (ADCs), and 12-bit digital-to-analog converters (DACs). The ST-Link/V3

embedded debugger and programmer facilitate the device's programming. The thermoelectric cooling module (23 mm × 23 mm × 2.1 mm, 2.4 ohms) is utilized for in-situ cooling treatment. A voltage divider was used to convert the resistance values of the temperature sensor into voltage signals, and a filter circuit could be used to remove circuit noise and electromagnetic interference.

Temperature resolution:

$$\frac{1\% \times \Delta T \times R_Z}{\Delta R} = \frac{1\% \times 20 \times 200k}{80k} = 0.5^\circ\text{C} \quad (3)$$

$$\begin{aligned} \Delta R &= R_{\max} - R_{\min} = 240\text{ k}\Omega - 160\text{ k}\Omega = 80\text{ k}\Omega \\ \Delta T &= 45^\circ\text{C} - 25^\circ\text{C} = 20^\circ\text{C} \\ R_Z &= \frac{R_{\max} - R_{\min}}{2} = \frac{240\text{ k}\Omega + 160\text{ k}\Omega}{2} = 200\text{ k}\Omega \end{aligned} \quad (4)$$

Display resolution:

$$\begin{aligned} 4096 \times \left( \frac{\frac{R_{\max}}{R'_z + R_{\max}} - \frac{R_{\min}}{R'_z + R_{\min}}}{\frac{240k}{200k+240k} - \frac{160k}{200k+160k}} \right) \\ = 4096 \times \left( \frac{\frac{240k}{200k+240k} - \frac{160k}{200k+160k}}{\frac{80k}{200k+240k}} \right) = 414 \\ \Delta T / 414 = 20^\circ\text{C} / 414 = 0.05^\circ\text{C} \end{aligned} \quad (5)$$

In the above equation,  $R_{\max}$  is 240 kΩ at the temperature of 25°C for the flexible thermal sensor,  $R_{\min}$  is 160 kΩ at temperature of 45°C for the flexible thermal sensor, and the measurement error of the instrument is 1%.  $R'_z$  represents the matching resistor in the circuit.

## Wearability application

Participants: 5 adult volunteers (18–65 years) and 2 infants (0–24 months) with parental consent. The study was approved by the Medical and Laboratory Animal Ethics Committee of Northwestern Polytechnical University. The data were obtained with the informed consent of all participants. Adults wear the device for 8 h (simulating nighttime use). Infants wear the device during naps and sleep, with caregivers recording observations of fussiness, skin redness, or attempts to remove the device. Data transmission and storage are based on the BLE4.0 protocol.

## Data availability

The data that support the findings of this study are available from the corresponding author upon reasonable request.

Received: 15 February 2025; Accepted: 18 August 2025;

Published online: 27 December 2025

## References

- Chung, H. U. et al. Binodal, wireless epidermal electronic systems with in-sensor analytics for neonatal intensive care. *Science* **363**, eaau0780 (2019).
- Chung, H. U. et al. Skin-interfaced biosensors for advanced wireless physiological monitoring in neonatal and pediatric intensive-care units. *Nat. Med.* **26**, 418–429 (2020).
- Yuan, M. et al. Soft electronics for advanced infant monitoring. *Mater. Today* **75**, 166–186 (2024).
- Yoo, J. Y. et al. Wireless broadband acousto-mechanical sensing system for continuous physiological monitoring. *Nat. Med.* **29**, 3137–3148 (2023).
- Inamori, G. et al. Neonatal wearable device for colorimetry-based real-time detection of jaundice with simultaneous sensing of vitals. *Sci. Adv.* **7**, eabe3793 (2021).
- Rwei, A. Y. et al. A wireless, skin-interfaced biosensor for cerebral hemodynamic monitoring in pediatric care. *Proc. Natl. Acad. Sci. USA* **117**, 31674–31684 (2020).
- Xu, K. et al. A wearable body condition sensor system with wireless feedback alarm functions. *Adv. Mater.* **33**, e2008701 (2021).
- Hong, S. et al. Wearable thermoelectrics for personalized thermoregulation. *Sci. Adv.* **5**, eaaw0536 (2019).
- Hu, R. et al. Emerging materials and strategies for personal thermal management. *Adv. Energy Mater.* **10**, 1903921 (2020).
- Wu, J. et al. Self-calibrated, sensitive, and flexible temperature sensor based on 3D chemically modified graphene hydrogel. *Adv. Electron. Mater.* **7**, 2001084 (2021).
- Wen, B. et al. Reduced graphene oxides: light-weight and high-efficiency electromagnetic interference shielding at elevated temperatures. *Adv. Mater.* **26**, 3484–3489 (2014).
- Zhang, H. et al. Graphene-enabled wearable sensors for healthcare monitoring. *Biosens. Bioelectron.* **197**, 113777 (2022).
- Trung, T. Q., Ramasundaram, S., Hwang, B. U. & Lee, N. E. An all-elastomeric transparent and stretchable temperature sensor for body-attachable wearable electronics. *Adv. Mater.* **28**, 502–509 (2016).
- Wang, Q. et al. Self-healable multifunctional electronic tattoos based on silk and graphene. *Adv. Funct. Mater.* **29**, 1808695 (2019).
- Zhu, C. X. et al. Stretchable temperature-sensing circuits with strain suppression based on carbon nanotube transistors. *Nat. Electron.* **1**, 183–190 (2018).
- Honda, W. et al. High-performance, mechanically flexible, and vertically integrated 3D carbon nanotube and InGaZnO complementary circuits with a temperature sensor. *Adv. Mater.* **27**, 4674–4680 (2015).
- Lee, J. H. et al. Rational design of all resistive multifunctional sensors with stimulus discriminability. *Adv. Funct. Mater.* **32**, 2107570 (2021).
- Lin, M. et al. A high-performance, sensitive, wearable multifunctional sensor based on rubber/CNT for human motion and skin temperature detection. *Adv. Mater.* **34**, 2107309 (2022).
- An, B. W., Heo, S., Ji, S., Bien, F. & Park, J. U. Transparent and flexible fingerprint sensor array with multiplexed detection of tactile pressure and skin temperature. *Nat. Commun.* **9**, 2458 (2018).
- Fan, W. et al. An Antisweat Interference and Highly Sensitive Temperature Sensor Based on Poly(3,4-ethylenedioxythiophene)-Poly(styrenesulfonate) Fiber Coated with Polyurethane/Graphene for Real-Time Monitoring of Body Temperature. *ACS Nano* **17**, 21073–21082 (2023).
- Pradhan, S. & Yadavalli, V. K. Photolithographically printed flexible silk/PEDOT:PSS temperature sensors. *ACS Appl. Electron. Mater.* **3**, 21–29 (2021).
- Hong, S. Y. et al. Stretchable active matrix temperature sensor array of polyaniline nanofibers for electronic skin. *Adv. Mater.* **28**, 930–935 (2016).
- Ge, G. et al. Muscle-inspired self-healing hydrogels for strain and temperature sensor. *ACS Nano* **14**, 218–228 (2020).
- Bang, J. et al. Highly sensitive temperature sensor: ligand-treated Ag nanocrystal thin films on PDMS with thermal expansion strategy. *Adv. Funct. Mater.* **29**, 1903047 (2019).
- He, W. et al. Polypyrrole/silver coaxial nanowire aero-sponges for temperature-independent stress sensing and stress-triggered Joule heating. *ACS Nano* **9**, 4244–4251 (2015).
- Wu, D. et al. Pt/Zn-TCPP nanozyme-based flexible immunoassay for dual-mode pressure-temperature monitoring of low-abundance proteins. *Anal. Chem.* **96**, 8740–8746 (2024).
- Huang, J. N. et al. Stretchable and heat-resistant protein-based electronic skin for human thermoregulation. *Adv. Funct. Mater.* **30**, 1910547 (2020).
- Hua, Q. et al. Skin-inspired highly stretchable and conformable matrix networks for multifunctional sensing. *Nat. Commun.* **9**, 244 (2018).
- Li, M. K. et al. Thermally conductive polyvinyl alcohol composite films via introducing hetero-structured MXene@silver fillers. *Nano Res.* **16**, 7820–7828 (2023).
- Zhang, S. P. et al. On-skin ultrathin and stretchable multifunctional sensor for smart healthcare wearables. *npj Flex. Electron.* **6**, 11 (2022).

31. Ge, G. et al. Ti(3)C(2)T(x) MXene-activated fast gelation of stretchable and self-healing hydrogels: a molecular approach. *ACS Nano* **15**, 2698–2706 (2021).

32. Liu, J. L. et al. Intelligent silk fibroin ionotronic skin for temperature sensing. *Adv. Mater. Technol.* **5**, 2000430 (2020).

33. Hao, S. W., Meng, L., Fu, Q. J., Xu, F. & Yang, J. Low-Temperature insensitivity and conformal adhesion zwitterionic hydrogels as electronic skin for strain and temperature responsiveness. *Chem. Eng. J.* **431**, 133782 (2022).

34. Yu, H. et al. Flexible temperature-pressure dual sensor based on 3D spiral thermoelectric Bi(2)Te(3) films. *Nat. Commun.* **15**, 2521 (2024).

35. Shin, J. et al. Sensitive wearable temperature sensor with seamless monolithic integration. *Adv. Mater.* **32**, 1905527 (2020).

36. Liu, Q. X. et al. A high-performances flexible temperature sensor composed of polyethyleneimine/reduced graphene oxide bilayer for real-time monitoring. *Adv. Mater. Technol.* **4**, 1800594 (2019).

37. Trung, T. Q. et al. A stretchable strain-insensitive temperature sensor based on free-standing elastomeric composite fibers for on-body monitoring of skin temperature. *ACS Appl. Mater. Inter.* **11**, 2317–2327 (2019).

38. Chhetry, A. et al. Black phosphorus@laser-engraved graphene heterostructure-based temperature-strain hybridized sensor for electronic-skin applications. *Adv. Funct. Mater.* **31**, 2007661 (2020).

39. Zhang, C. et al. Dopamine-triggered hydrogels with high transparency, self-adhesion, and thermoresponse as skinlike sensors. *ACS Nano* **15**, 1785–1794 (2021).

40. Wang, Y. et al. Ti(3)C(2)T(x) MXene-based flexible piezoresistive physical sensors. *ACS Nano* **16**, 1734–1758 (2022).

41. Wang, W. C. et al. Strain-insensitive intrinsically stretchable transistors and circuits. *Nat. Electron.* **4**, 143–150 (2021).

42. Zhao, Y. et al. Soft strain-insensitive bioelectronics featuring brittle materials. *Science* **378**, 1222–1227 (2022).

43. Li, A. et al. High performance magnesium-based plastic semiconductors for flexible thermoelectrics. *Nat. Commun.* **15**, 5108 (2024).

44. Powell, A. V., Vaqueiro, P., Tippireddy, S. & Prado-Gonjal, J. Exploiting chemical bonding principles to design high-performance thermoelectric materials. *Nat. Rev. Chem.* **9**, 241–260 (2025).

45. Zhang, Q. H., Deng, K. F., Wilkens, L., Reith, H. & Nielsch, K. Micro-thermoelectric devices. *Nat. Electron.* **5**, 333–347 (2022).

46. Mao, J., Chen, G. & Ren, Z. Thermoelectric cooling materials. *Nat. Mater.* **20**, 454–461 (2021).

47. Zhang, S. et al. Solid-state cooling by elastocaloric polymer with uniform chain-lengths. *Nat. Commun.* **13**, 9 (2022).

48. Ma, R. et al. Highly efficient electrocaloric cooling with electrostatic actuation. *Science* **357**, 1130–1134 (2017).

49. Wang, Y. et al. A high-performance solid-state electrocaloric cooling system. *Science* **370**, 129–133 (2020).

50. Moya, X., Kar-Narayan, S. & Mathur, N. D. Caloric materials near ferroic phase transitions. *Nat. Mater.* **13**, 439–450 (2014).

51. Kishore, R. A., Nozariasbmarz, A., Poudel, B., Sanghadasa, M. & Priya, S. Ultra-high performance wearable thermoelectric coolers with less materials. *Nat. Commun.* **10**, 1765 (2019).

52. Deng, Y. et al. Fast Gelation of Ti(3)C(2)T(x) MXene Initiated by Metal Ions. *Adv. Mater.* **31**, 1902432 (2019).

53. He, H. et al. Salt-induced ductilization and strain-insensitive resistance of an intrinsically conducting polymer. *Sci. Adv.* **8**, eabq8160 (2022).

54. Xu, Y. et al. Phase-separated porous nanocomposite with ultralow percolation threshold for wireless bioelectronics. *Nat. Nanotechnol.* **19**, 1158–1167 (2024).

55. Hao, S., Fu, Q., Meng, L., Xu, F. & Yang, J. A biomimetic laminated strategy enabled strain-interference free and durable flexible thermistor electronics. *Nat. Commun.* **13**, 6472 (2022).

56. Ma, T. et al. A bioinspired interface design for improving the strength and electrical conductivity of graphene-based fibers. *Adv. Mater.* **30**, 1706435 (2018).

57. Sun, W. B. et al. Nacre-inspired bacterial cellulose/mica nanopaper with excellent mechanical and electrical insulating properties by biosynthesis. *Adv. Mater.* **35**, 2300241 (2023).

58. Zhang, X., Wu, K., Ni, Y. & He, L. Anomalous inapplicability of nacre-like architectures as impact-resistant templates in a wide range of impact velocities. *Nat. Commun.* **13**, 7719 (2022).

59. Liu, H. et al. Approaching intrinsic dynamics of MXenes hybrid hydrogel for 3D printed multimodal intelligent devices with ultrahigh superelasticity and temperature sensitivity. *Nat. Commun.* **13**, 3420 (2022).

60. Li, X. et al. MXene chemistry, electrochemistry and energy storage applications. *Nat. Rev. Chem.* **6**, 389–404 (2022).

61. Huang, X. et al. High-stretchability and low-hysteresis strain sensors using origami-inspired 3D mesostructures. *Sci. Adv.* **9**, eadh9799 (2023).

62. Jiang, Y. et al. Wireless, closed-loop, smart bandage with integrated sensors and stimulators for advanced wound care and accelerated healing. *Nat. Biotechnol.* **41**, 652–662 (2023).

63. Miao, L. et al. Comfortable wearable thermoelectric generator with high output power. *Nat. Commun.* **15**, 8516 (2024).

64. Yang, Q. et al. Flexible thermoelectrics based on ductile semiconductors. *Science* **377**, 854–858 (2022).

65. Reeder, J. T. et al. Soft, bioresorbable coolers for reversible conduction block of peripheral nerves. *Science* **377**, 109–115 (2022).

66. Urisarri, A. et al. BMP8 and activated brown adipose tissue in human newborns. *Nat. Commun.* **12**, 5274 (2021).

67. Zhang, X. et al. Flexible temperature sensor with high reproducibility and wireless closed-loop system for decoupled multimodal health monitoring and personalized thermoregulation. *Adv. Mater.* **36**, 2407859 (2024).

68. Madhvapathy, S. R. et al. Miniaturized implantable temperature sensors for the long-term monitoring of chronic intestinal inflammation. *Nat. Biomed. Eng.* **8**, 1040–1052 (2024).

69. Zheng, X. T. et al. Battery-free and AI-enabled multiplexed sensor patches for wound monitoring. *Sci. Adv.* **9**, eadg6670 (2023).

70. Chen, X. et al. Non-invasive activation of intratumoural gene editing for improved adoptive T-cell therapy in solid tumours. *Nat. Nanotechnol.* **18**, 933–944 (2023).

71. Yang, M. Z. et al. Roll-to-roll fabricated polymer composites filled with subnanosheets exhibiting high energy density and cyclic stability at 200 °C. *Nat. Energy* **9**, 143–153 (2024).

72. Shao, Y. et al. Room-temperature high-precision printing of flexible wireless electronics based on MXene inks. *Nat. Commun.* **13**, 3223 (2022).

73. Zou, K. et al. Electronic cooling and energy harvesting using ferroelectric polymer composites. *Nat. Commun.* **15**, 6670 (2024).

74. Liu, C. et al. Multi-Interface Engineering of MXenes for Self-Powered Wearable Devices. *Adv. Mater.* **36**, 2403791 (2024).

75. Zhang, B. et al. Nature-inspired interfacial engineering for energy harvesting. *Nat. Rev. Electr. Eng.* **1**, 218–233 (2024).

76. Zhang, B. et al. A three-dimensional liquid diode for soft, integrated permeable electronics. *Nature* **628**, 84–92 (2024).

77. Joyce, P. et al. A translational framework to DELIVER nanomedicines to the clinic. *Nat. Nanotechnol.* **19**, 1597–1611 (2024).

## Acknowledgements

We thank the funding support from the Natural Science Foundation of Shaanxi Province (No. D5110240073).

## Author contributions

Y.Y. and H.Q.Z. conceived and designed the experiments. X.J.H. and H.Q.Z. prepared the temperature sensor and cooling module, conducted characterization, performance testing, data analysis, and drafted the paper.

Y.H. and Y.C.H. completed finite element analysis. Y.X.S. handled XPS data analysis. Y.F.G. supported the verification of MXene film strain insensitivity experimental data. P.L. coordinated the development of the thermoelectric cooling module and provided experimental equipment for testing the thermoelectric module's performance. H.Q.Z., P.L., F.X., and Y.Y. revised the paper. All authors discussed the results and commented on the manuscript.

### Competing interests

The authors declare no competing interests.

### Additional information

**Supplementary information** The online version contains supplementary material available at <https://doi.org/10.1038/s41528-025-00476-7>.

**Correspondence** and requests for materials should be addressed to Huiqing Zhang, Peng Li, Feng Xu or Yao Yao.

**Reprints and permissions information** is available at <http://www.nature.com/reprints>

**Publisher's note** Springer Nature remains neutral with regard to jurisdictional claims in published maps and institutional affiliations.

**Open Access** This article is licensed under a Creative Commons Attribution-NonCommercial-NoDerivatives 4.0 International License, which permits any non-commercial use, sharing, distribution and reproduction in any medium or format, as long as you give appropriate credit to the original author(s) and the source, provide a link to the Creative Commons licence, and indicate if you modified the licensed material. You do not have permission under this licence to share adapted material derived from this article or parts of it. The images or other third party material in this article are included in the article's Creative Commons licence, unless indicated otherwise in a credit line to the material. If material is not included in the article's Creative Commons licence and your intended use is not permitted by statutory regulation or exceeds the permitted use, you will need to obtain permission directly from the copyright holder. To view a copy of this licence, visit <http://creativecommons.org/licenses/by-nc-nd/4.0/>.

© The Author(s) 2025